Joint Optimization of Sparse MIMO Arrays and Imaging Methods

Okyanus Oral* and Figen S. Oktem
Department of Electrical Engineering, METU, Ankara, 06800, Turkey
Email: figeno@metu.edu.tr

***Abstract*—Sparse multiple-input multiple-output (MIMO) radar imaging systems provide high-resolution reconstructions with reduced hardware complexity, finding broad applications ranging from medical imaging to security. The image quality of these systems heavily depends on both the array design and the reconstruction algorithm used. While existing approaches usually treat these components separately, we propose a novel framework to jointly optimize MIMO array configurations and reconstruction algorithms. This joint optimization, performed in an end-to-end manner, leads to MIMO imaging systems specifically optimized for enhanced reconstruction quality. Through numerical simulations for a large-scale near-field microwave imaging application, we show that our approach consistently outperforms commonly used sparse arrays across various reconstruction methods.**

***Index Terms*—MIMO radar imaging, end-to-end optimization, deep learning, computational imaging.**

I. Introduction

Radar imaging systems find extensive use in diverse fields, including environmental monitoring, medical diagnostics, security screening, through-wall imaging, and non-destructive evaluation [1], [2]. Traditional radar systems typically rely on densely populated arrays with closely spaced antenna elements to avoid grating lobes and achieve high-resolution images. In such monostatic designs, cross-range and down-range resolutions are fundamentally limited by antenna aperture and bandwidth. Achieving higher resolutions thus necessitates increased hardware complexity and cost, making these systems less practical for cost-sensitive or large-scale applications such as autonomous vehicles.

Sparse multiple-input multiple-output (MIMO) arrays have emerged as promising alternatives for high-resolution radar imaging, providing advantages in reduced hardware complexity, lower cost, and faster data acquisition [3], [4], [5], [6], [7], [8]. Unlike traditional monostatic arrays, sparse MIMO configurations spatially distribute transmit and receive antennas, resulting in significant decrease in system complexity. While various sparse array topologies have been proposed, traditional array design methods often focus on indirect performance metrics, such as the point-spread function or virtual array distribution [9], [4], [10], [11], [12], [13], [14], [15]. Since existing design approaches do not explicitly incorporate the final image quality into the optimization process, they typically do not explicitly optimize the image quality achieved with these imaging systems.

Radar imaging inherently requires solving an ill-posed inverse problem to reconstruct the complex-valued reflectivity of the scene from sparse measurements. Consequently, image reconstruction quality strongly depends on both the antenna array topology and the reconstruction method employed. However, existing research typically focuses on either optimizing the array design or improving image reconstruction algorithms, without jointly addressing both aspects [4], [10], [8], [11], [16], [17], [18], [19].

Recently, inverse-theoretic methods emerged to explicitly incorporate image reconstruction quality in array optimization. For instance, Bayesian estimation framework was used to optimize antenna positions using a greedy selection algorithm [8], and compressed sensing-based methods were employed to obtain a binary sampling pattern for antenna positions [17], [16]. However, while these methods optimize arrays to improve the imaging performance of specific reconstruction algorithms, they still lack a fully data-driven, end-to-end (E2E) optimization framework.

Recent advancements in computational imaging have shown that joint optimization of system design parameters and reconstruction methods significantly improves performance across various imaging domains [20], [21], [22], [23], [24]. Such end-to-end (E2E) frameworks successfully enhanced imaging quality by simultaneously optimizing the imaging hardware and software in diverse fields, including spectral imaging, microscopy, medical imaging, and seismic imaging [21], [23]. However, there is limited work on jointly optimizing both the MIMO array and the reconstruction method in a data-driven end-to-end fashion [25], especially for large-scale 3D radar imaging with flexible reconstruction methods and 2D aperture configurations.

In this work, we propose a general and efficient framework for end-to-end optimization of MIMO antenna arrays and image reconstruction algorithms for radar imaging. By formulating differentiable computation graphs of the complete imaging pipeline, from measurement simulation to reconstruction, we leverage gradient-based optimization methods to jointly optimize antenna configurations and reconstruction algorithms. We validate our framework on a 3D near-field microwave imaging scenario using different reconstruction methods and large synthetic dataset. Experimental results demonstrate that

*At the time of this study, O. Oral was with the Department of Electrical Engineering, METU, Turkey. He is now with the Doctoral Programme in Computer Science and Computer Engineering, University of Luxembourg, Luxembourg.

our optimized MIMO arrays consistently outperform common sparse array designs, highlighting the importance of joint optimization for enhancing radar imaging quality.

II. Observation Model

This section describes a general observation model for MIMO radar imaging, applicable to both near- and far-field scenarios. A sample observation geometry is given in Figure 1. As depicted, a planar MIMO array is placed at $z = 0$, consisting of spatially distributed transmit and receive antennas whose configurations will be optimized. Each transmit antenna sends a radar pulse and the scattered field is then captured by all receive antennas.

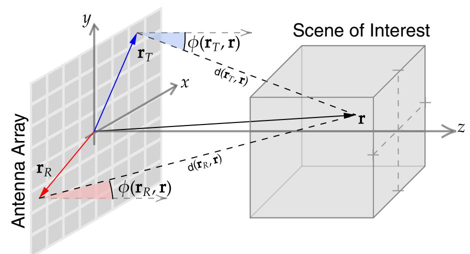

Fig. 1: Sample Observation Geometry

Under the Born approximation, the scattered field measured by the MIMO radar system can be formulated as follows [26], [19]:

$$y(\mathbf{r}_T, \mathbf{r}_R, k) = p(k) \sum_{x,y,z} \frac{e^{-jk(d(\mathbf{r}_T,\mathbf{r})+d(\mathbf{r}_R,\mathbf{r}))}}{4\pi \; d(\mathbf{r}_T, \mathbf{r}) \; d(\mathbf{r}_R, \mathbf{r})} s(\mathbf{r}), \tag{1}$$

where $y(\mathbf{r}_T, \mathbf{r}_R, k)$ denotes the frequency-domain measurement obtained using a specific transmitter-receiver pair located at $\mathbf{r}_T$ and $\mathbf{r}_R$, respectively, and $s(\mathbf{r})$ represents the discretized reflectivity distribution of the scene at voxel $\mathbf{r} = [x, y, z]^T$. The function $p(k)$ is the temporal Fourier transform of the transmitted pulse with $k = \frac{2\pi}{c} f$ denoting the frequency-wavenumber, f denoting the temporal frequency, and c denoting the speed of light. Distances from a given voxel $\mathbf{r}$ to transmit and receive antennas are defined as $d(\mathbf{r}_T, \mathbf{r}) = \|\mathbf{r}_T - \mathbf{r}\|_2$ and $d(\mathbf{r}_R, \mathbf{r}) = \|\mathbf{r}_R - \mathbf{r}\|_2$ respectively. The attenuation factor $1/(d(\mathbf{r}_R, \mathbf{r}) d(\mathbf{r}_T, \mathbf{r}))$ drops in the special case of far-field imaging.

This discrete observation model can be compactly written as

$$\mathbf{y} = \mathbf{A}\mathbf{s} + \mathbf{w}. \tag{2}$$

where $\mathbf{s} \in \mathbb{C}^N$ is the discretized reflectivity vector with N denoting the number of image voxels, and $\mathbf{y} \in \mathbb{C}^M$ are the corresponding noisy measurement vector acquired at different antenna locations and frequency steps with M denoting the total number of measurements. The measurement matrix $\mathbf{A} \in \mathbb{C}^{M \times N}$ has entries given by

$$\mathbf{A}_{m,n} = p(k_m) \frac{e^{-jk_m(d(\mathbf{r}_{T_m},\mathbf{r}_n)+d(\mathbf{r}_{R_m},\mathbf{r}_n))}}{4\pi \; d(\mathbf{r}_{T_m}, \mathbf{r}_n) \; d(\mathbf{r}_{R_m}, \mathbf{r}_n)}, \tag{3}$$

which indicates the contribution of the nth voxel, located at $\mathbf{r}_n$, to the mth measurement taken with the antenna pair $(\mathbf{r}_{T_m}, \mathbf{r}_{R_m})$ at frequency $\frac{c}{2\pi} k_m$. The additive noise vector $\mathbf{w} \in \mathbb{C}^M$ is modeled as white Gaussian, which is typically a valid assumption in realistic scenarios. Thus, each entry of $\mathbf{w}$ has independent and identically distributed Gaussian characteristics with variance σ_w^2. Each measurement indexed by m corresponds to a unique combination of transmitting and receiving antenna locations and frequency step. Additionally, each voxel indexed by n refers to a distinct position within the discretized three-dimensional scene.

III. Developed Method

This section presents our proposed framework for jointly optimizing the MIMO array configuration and imaging algorithm. In this joint optimization approach, our goal is to simultaneously optimize the array parameters, μ, together with the parameters of the imaging algorithm, θ. The joint optimization problem is formulated as a constrained minimization:

$$\hat{\theta}, \hat{\mu} = \arg\min_{\theta,\mu} \sum_{\mathbf{s} \in \chi} \frac{1}{N_\chi} \mathcal{L}(\mathbf{s}, \hat{\mathbf{s}}) \tag{4}$$
$$\text{subject to} \;\; \hat{\mathbf{s}} = \mathcal{D}_{\theta,\mu}(\mathbf{A}_\mu \mathbf{s} + \mathbf{w}) \;, \; \mu \in \Omega$$

where χ denotes a training dataset of size N_χ consisting of reflectivity images. The function $\mathcal{L}(\cdot, \cdot)$ is the cost measuring the fidelity of the reconstructed reflectivity $\hat{\mathbf{s}}$ to the ground truth $\mathbf{s}$. Additionally, $\mathbf{A}_\mu$ denotes the measurement matrix parametrized by the array design parameters μ, and the image reconstruction is performed via algorithm $\mathcal{D}_{\theta,\mu}(\mathbf{y})$ whose parameters are denoted by θ. The constraint set for the antenna parameters is denoted by Ω.

Learning-based reconstruction methods generally have millions of parameters, making second-order optimization methods computationally prohibitive. To handle this large-scale optimization problem efficiently, we employ the first-order Projected Gradient Descent (PGD) method [27]. The iterative update rules for PGD are given by:

$$\theta^{l+1} = \theta^l - \eta_\theta \frac{\partial}{\partial \theta^l} \left(\frac{1}{N_\chi} \sum_{s \in \chi} \mathcal{L}(\mathbf{s}, \hat{\mathbf{s}}) \right) \tag{5}$$

$$\mu^{l+1} = \text{Proj}_\Omega \left(\mu^l - \eta_\mu \frac{\partial}{\partial \mu^l} \left(\frac{1}{N_\chi} \sum_{s \in \chi} \mathcal{L}(\mathbf{s}, \hat{\mathbf{s}}) \right) \right) \tag{6}$$

where η_μ and η_θ are the step sizes for array and algorithm parameter updates, respectively.The projection operator $\text{Proj}_\Omega(\cdot)$ onto the array constraint set Ω is defined as:

$$\text{Proj}_\Omega(\bar{\mu}) \triangleq \arg\min_{\mu} \|\bar{\mu} - \mu\|_2 \text{ s.t. } \mu \in \Omega. \tag{7}$$

This operator corresponds to the proximal mapping enforcing antenna array constraints. For instance, when optimizing antenna positions, Ω represents the allowed aperture area, and the projection operator corresponds to correcting the positions of antennas if they lie outside the predefined aperture area by assigning the closest point inside the aperture to its position.

The iterative optimization defined by (5) and (6) is implemented in the PyTorch environment, utilizing automatic differentiation for efficient gradient computation. The block diagram illustrating the computation graph constructed for automatic differentiation is provided in Figure 2.

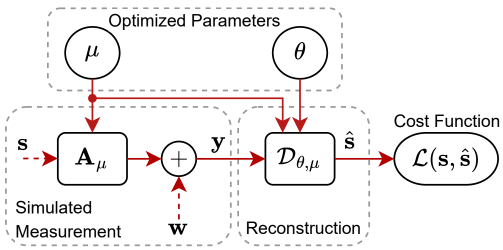

Fig. 2: Block diagram for E2E optimization. Solid lines denote the differentiated path for back-propagation.

IV. Results

We demonstrate the effectiveness and versatility of the developed joint optimization framework for 3D microwave imaging. In our simulations, we consider an imaging volume of 30 cm $\times$ 30 cm $\times$ 30 cm located 50 cm away from the antenna array. Given a predefined square-shaped antenna aperture of width 30 cm, we optimize positions of transmit and receive antennas jointly with the reconstruction algorithm. The operating frequency is swept from 4 to 16 GHz with 15 steps. Accordingly, the voxel sizes along x, y, and z directions are set to 1.25cm, 1.25cm, and 0.625cm respectively, to closely approximate the theoretical resolution expected for the non-compressive case [26]. This discretization results in an imaging volume of $25 \times 25 \times 49$ voxels.

For sparse MIMO array optimization, the total antenna count is fixed as 25 to explore different numbers of transmit and receive antennas ($N_{Tx} + N_{Rx} = 25$). The highest number of measurements, and therefore lowest compression ratio, occurs when the number of transmit and receive elements, i.e. N_{Tx} and N_{Rx}, are approximately equal. We explicitly compare our optimized arrays with some commonly used arrays [4], such as the the Mill's cross array (MCA) with 12 transmit and 13 receive antennas along diagonals, uniform rectangular (URA) and ring spiral (RSA) arrays with 9 transmit and 16 receive antennas.

Measurements are simulated on synthetic datasets of 3D extended targets from [28], consisting of 800 training, 100 validation, and 100 test samples. Each reflectivity voxel includes random phase to mimic practical imaging conditions. Measurements include additive white Gaussian noise, with SNR levels randomly selected in each optimization iteration between 0 and 30 dB.

Considering varying computational demands across applications, we perform joint optimization with different imaging methods, including traditional direct inversion, regularized unrolling-based methods, and deep learning approaches. Specifically, we select:

- Kirchhoff migration (KM) [29], a parameter-free baseline method involving direct inversion.
- An unrolled ℓ_1 regularization-based method (U-ℓ_1) [30], [31], [32], where step sizes and soft-threshold parameters are optimized for $L = 3$ unrolling steps, totaling 6 parameters.
- Deep2S [28], a deep learning-based reconstruction method where the parameters are the weights of the employed neural network architecture, comprising 1,356,641 parameters.

The cost function in (4) is chosen as the mean squared error computed on normalized magnitudes of reflectivity images. To enhance computational efficiency, we substitute the gradient descent steps with a single iteration of the Adam algorithm [33], set the batch size to 16, and train for up to 2000 epochs, employing early stopping when validation loss stagnates for 50 epochs.

For Deep2S, neural network weights (1,356,641 parameters) are trained jointly with antenna parameters. Initial learning rates are set as 10^{-2} for antenna parameters and 10^{-3} for the neural network weights. For the U-ℓ_1 method, separate initial learning rates are chosen for step-size (10^{-6}) and soft-threshold parameters (10^{-4}). A learning rate scheduler reduces the learning rate by a factor of 10 upon stagnation of validation loss. Joint optimization takes approximately 2 hours on a NVIDIA GeForce RTX 3080 Ti GPU using PyTorch 1.12.0 with CUDA Toolkit 11.6.0 in Python 3.10.6.

To analyze the performance of jointly optimized arrays for various transmitter/receiver configurations, we consider $N_{Tx} + N_{Rx} = 25$ and vary the number of antennas from $(N_{Tx}, N_{Rx}) = (1, 24)$ to $(12, 13)$ since configurations with $N_{Tx} > 12$ are redundant due to array symmetry. Optimization is performed separately for KM, U-ℓ_1, and Deep2S reconstruction methods. Average test performance over measurement SNRs from 0 dB to 30 dB is shown in Fig. 3 as a function of number of transmitters used in the design, alongside baseline arrays MCA, URA, and RSA denoted with marks $\times$, $\square$ and $\bigcirc$, respectively.

Results indicate that optimized arrays consistently outperform these standard designs up to a PSNR of 2 dB. Furthermore, all reconstruction methods reach maximum performance at $N_{Tx} = 12$, $N_{Rx} = 13$, corresponding to the lowest compression case. However, improvements become marginal beyond $N_{Tx} = 6$, suggesting minimal practical benefit from further increasing transmit antennas and hence the acquisition time. The results also illustrate notable improvements in image quality, especially for the KM method, which achieves more than 2.3 dB improvement over baseline arrays. Similarly, Deep2S-based optimization achieves more than 1 dB PSNR improvement compared to the next-best performing array (URA), demonstrating the effectiveness of joint optimization.

The jointly optimized arrays for Deep2S, Kirchhoff migration, and ℓ_1 regularization, along with their virtual arrays, are shown in Fig. 4. As seen, different reconstruction algorithms

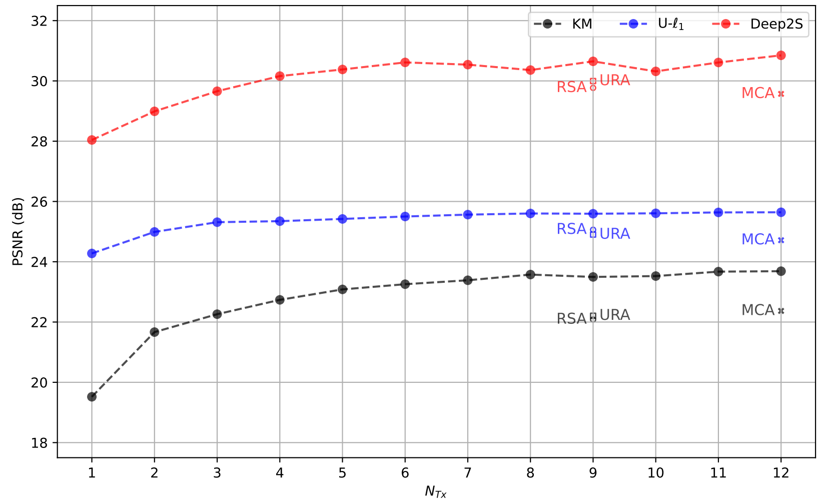

Fig. 3: Average test performance across different measurement SNRs vs. number of transmitter antennas ($N_{Rx} = 25 - N_{Tx}$). Commonly used MIMO arrays (Mill's Cross, Uniform Rectangular, Ring Spiral) and optimized arrays are compared.

yield notably distinct array configurations, highlighting that optimal array design strongly depends on the selected imaging algorithm. Specifically, Deep2S yields a configuration where transmit antennas are arranged in a grid-like fashion similarly to URA but with the difference of having transmit antennas at the aperture boundaries. Moreover, receive antennas are present both at the boundaries and near the center, which results in virtual antenna elements sampling the entire aperture. In fact, its virtual array shares similarities with RSA since the distribution of the virtual antennas of both arrays is non-periodic and more dense at the center.

V. Conclusion

This paper introduced a novel joint optimization framework for sparse MIMO radar imaging, simultaneously optimizing antenna array configurations and image reconstruction algorithms. The proposed approach is efficient and general, accommodating different imaging methods including traditional direct inversion, iterative regularized reconstruction, and deep learning-based reconstruction. Numerical experiments demonstrated that our optimized systems consistently outperform traditional MIMO arrays, achieving superior imaging quality across different SNR levels and antenna configurations.

The developed framework not only offers performance improvements but also provides valuable insights into how array design should align with reconstruction algorithms. Future extensions of this work could include integrating different practical considerations into optimization such as antenna patterns or employing richer datasets for increased robustness.

Acknowledgment

This study was funded by Scientific and Technological Research Council of Turkey (TUBITAK) under the Grant Number 120E505.

References

[1] S. S. Ahmed, A. Schiessl, F. Gumbmann, M. Tiebout, S. Methfessel, and L.-P. Schmidt, "Advanced microwave imaging," *IEEE Microwave Magazine*, vol. 13, no. 6, pp. 26–43, 2012.

[2] L. C. Potter, E. Ertin, J. T. Parker, and M. Cetin, "Sparsity and compressed sensing in radar imaging," *Proceedings of the IEEE*, vol. 98, no. 6, pp. 1006–1020, 2010.

[3] X. Zhuge and A. G. Yarovoy, "A sparse aperture MIMO-SAR-based UWB imaging system for concealed weapon detection," *IEEE Trans. Geosci. Remote Sens.*, vol. 49, no. 1, pp. 509–518, 2010.

[4] X. Zhuge and G. Yarovoy, Alexander, "Study on two-dimensional sparse MIMO UWB arrays for high resolution near-field imaging," *IEEE Trans. Antennas Propag.*, vol. 60, no. 9, pp. 4173–4182, 2012.

[5] S. S. Ahmed, A. Schiess, and L.-P. Schmidt, "Near field mm-wave imaging with multistatic sparse 2D-arrays," in *2009 European Radar Conference (EuRAD)*. IEEE, 2009, pp. 180–183.

[6] M. E. Yanik and M. Torlak, "Near-field MIMO-SAR millimeter-wave imaging with sparsely sampled aperture data," *IEEE Access*, vol. 7, pp. 31 801–31 819, 2019.

[7] E. Anadol, I. Seker, S. Camlica, T. O. Topbas, S. Koc, L. Alatan, F. Oktem, and O. A. Civi, "UWB 3D near-field imaging with a sparse MIMO antenna array for concealed weapon detection," in *Radar Sensor Technology XXII*, vol. 10633. SPIE, 2018, pp. 458–472.

[8] M. B. Kocamis and F. S. Oktem, "Optimal design of sparse MIMO arrays for near-field ultrawideband imaging," in *2017 25th European Signal Processing Conference (EUSIPCO)*. IEEE, 2017, pp. 1952–1956.

[9] Y. Liu, Z. Nie, and Q. H. Liu, "Reducing the number of elements in a linear antenna array by the matrix pencil method," *IEEE Transactions on Antennas and Propagation*, vol. 56, no. 9, pp. 2955–2962, 2008.

[10] Q. Cheng, Y. Liu, H. Zhang, and Y. Hao, "A generic spiral MIMO array design method for short-range UWB imaging," *IEEE Antennas and Wireless Propagation Letters*, vol. 19, no. 5, pp. 851–855, 2020.

[11] H. Cetinkaya, S. Kueppers, R. Herschel, and N. Pohl, "Millimeter-wave MIMO array based on semi-circular topology," *IEEE Sensors Journal*, vol. 20, no. 14, pp. 7740–7749, 2020.

[12] B. Gonzalez-Valdes, G. Allan, Y. Rodriguez-Vaqueiro, Y. Alvarez, S. Mantzavinos, M. Nickerson, B. Berkowitz, J. Martı, F. Las-Heras, C. M. Rappaport *et al.*, "Sparse array optimization using simulated annealing and compressed sensing for near-field millimeter wave imaging," *IEEE Transactions on Antennas and Propagation*, vol. 62, no. 4, pp. 1716–1722, 2013.

[13] Q. An, A. Hoorfar, H. Lv, and J. Wang, "Task-specific sparse MIMO array design for TWRI using multi-objective CMA-ES," in *2021 XXXIVth General Assembly and Scientific Symposium of the International Union of Radio Science (URSI GASS)*, 2021, pp. 1–4.

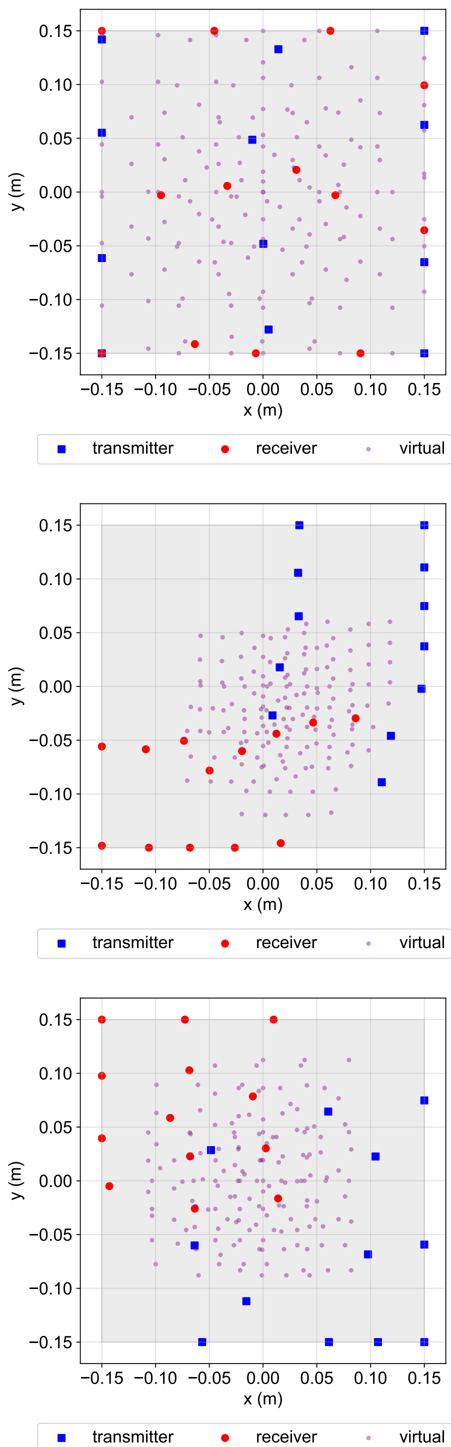

Fig. 4: Jointly optimized arrays with Deep2S, KM, and ℓ_1 regularization (top to below), using 12 transmit and 13 receive antennas.

[14] K. Tan, S. Wu, Y. Wang, S. Ye, J. Chen, and G. Fang, "A novel two-dimensional sparse MIMO array topology for UWB short-range imaging," *IEEE Antennas and Wireless Propagation Letters*, vol. 15, pp. 702–705, 2016.

[15] B. Yang, X. Zhuge, A. Yarovoy, and L. Ligthart, "UWB MIMO antenna array topology design using PSO for through dress near-field imaging," in *2008 38th European Microwave Conference*. IEEE, 2008, pp. 1620–1623.

[16] S. Wang, S. Li, B. Ren, K. Miao, G. Zhao, and H. Sun, "Convex optimization-based design of sparse arrays for 3-D near-field imaging," *IEEE Sensors Journal*, vol. 23, no. 9, pp. 9640–9648, 2023.

[17] S. Wang, S. Li, A. Hoorfar, K. Miao, G. Zhao, and H. Sun, "Compressive sensing based sparse MIMO array synthesis for wideband near-field millimeter-wave imaging," *IEEE Transactions on Aerospace and Electronic Systems*, 2023.

[18] M. B. Alver, A. Saleem, and M. Çetin, "Plug-and-play synthetic aperture radar image formation using deep priors," *IEEE Trans. Comput. Imag.*, vol. 7, pp. 43–57, 2021.

[19] O. Oral and F. S. Oktem, "Plug-and-play regularization on magnitude with deep priors for 3D Near-Field MIMO imaging," *IEEE Transactions on Computational Imaging*, vol. 10, pp. 762–773, 2024.

[20] D. Mengu, M. S. S. Rahman, Y. Luo, J. Li, O. Kulce, and A. Ozcan, "At the intersection of optics and deep learning: statistical inference, computing, and inverse design," *Adv. Opt. Photon.*, vol. 14, no. 2, pp. 209–290, Jun 2022.

[21] L. Wang, T. Zhang, Y. Fu, and H. Huang, "HyperReconNet: Joint coded aperture optimization and image reconstruction for compressive hyperspectral imaging," *IEEE Transactions on Image Processing*, vol. 28, no. 5, pp. 2257–2270, 2019.

[22] C. D. Bahadir, A. Q. Wang, A. V. Dalca, and M. R. Sabuncu, "Deep-learning-based optimization of the under-sampling pattern in MRI," *IEEE Transactions on Computational Imaging*, vol. 6, pp. 1139–1152, 2020.

[23] M. R. Kellman, E. Bostan, N. A. Repina, and L. Waller, "Physics-based learned design: optimized coded-illumination for quantitative phase imaging," *IEEE Transactions on Computational Imaging*, vol. 5, no. 3, pp. 344–353, 2019.

[24] A. Hernandez-Rojas and H. Arguello, "3D geometry design via end-to-end optimization for land seismic acquisition," in *2022 IEEE International Conference on Image Processing (ICIP)*, 2022, pp. 4053–4057.

[25] T. Weiss, N. Peretz, S. Vedula, A. Feuer, and A. Bronstein, "Joint optimization of system design and reconstruction in MIMO radar imaging," in *2021 IEEE 31st International Workshop on Machine Learning for Signal Processing (MLSP)*. IEEE, 2021, pp. 1–6.

[26] X. Zhuge and A. G. Yarovoy, "Three-dimensional near-field MIMO array imaging using range migration techniques," *IEEE Trans. Image Process.*, vol. 21, no. 6, pp. 3026–3033, 2012.

[27] S. Boyd, L. Xiao, and A. Mutapcic, "Subgradient methods," *lecture notes of EE392o, Stanford University, Autumn Quarter*, vol. 2004, no. 01, 2003.

[28] I. Manisali, O. Oral, and F. S. Oktem, "Efficient physics-based learned reconstruction methods for real-time 3D near-field MIMO radar imaging," *Digital Signal Processing*, vol. 144, p. 104274, 2024.

[29] X. Zhuge, A. G. Yarovoy, T. Savelyev, and L. Ligthart, "Modified Kirchhoff migration for UWB MIMO array-based radar imaging," *IEEE Trans. Geosci. Remote Sens.*, vol. 48, no. 6, pp. 2692–2703, 2010.

[30] V. Monga, Y. Li, and Y. C. Eldar, "Algorithm unrolling: Interpretable, efficient deep learning for signal and image processing," *IEEE Signal Processing Magazine*, vol. 38, no. 2, pp. 18–44, 2021.

[31] J. Zhang and B. Ghanem, "ISTA-Net: Interpretable optimization-inspired deep network for image compressive sensing," in *2018 IEEE/CVF Conference on Computer Vision and Pattern Recognition*, 2018, pp. 1828–1837.

[32] M. Wang, S. Wei, J. Liang, X. Zeng, C. Wang, J. Shi, and X. Zhang, "RMIST-Net: joint range migration and sparse reconstruction network for 3-D mmW imaging," *IEEE Trans. Geosci. Remote Sens.*, vol. 60, pp. 1–17, 2021.

[33] D. P. Kingma and J. Ba, "Adam: A method for stochastic optimization," *arXiv preprint arXiv:1412.6980*, 2014.